EVALUATION OF A CAMBER MORPHING CONCEPT BASED ON CONTROLLED FLEXIBILITY

Guclu Seber[1], Evren Sakarya[2], Tolga E. Insuyu[3], Melin Sahin[4], Serkan Ozgen[5], Yavuz Yaman[6]

Aerospace Engineering Department
Middle East Technical University, Ankara, Turkey

e-mail: [1]gseber@ae.metu.edu.tr, [2]esakarya@ae.metu.edu.tr, [3]tinsuyu@ae.metu.edu.tr, [4]melin@ae.metu.edu.tr, [5]sozgen@ae.metu.edu.tr, [6]yyaman@metu.edu.tr

Keywords: Morphing Aircraft, Hingeless Control Surface, Finite Element Method, Nonlinear Contact Analysis, CFD based aerodynamics.

Abstract. In this study, a camber morphing concept is introduced as an alternative to existing plain flap or aileron type hinged control surfaces used in wings. This concept functions by flexing the skin panels and imposing a sliding motion in the semi-open secondary wing structure. Thus, the desired aerodynamic camber is obtained by means of a hingeless control surface. To investigate the structural aspects, static nonlinear finite element analyses are performed for a representative morphing wing section by using MSC® NASTRAN. In the models created, double sided contact surfaces are defined to include the relative motion between parts and to prevent the separation of the upper and lower skin panels. By using the results obtained from the structural analyses, contours of the morphed sections are determined. This information is then used to define the aerodynamic geometries in the CFD based 2D solutions obtained using ANSYS® FLUENT. In the aerodynamic analyses performed, the aerodynamics coefficients as well as the chordwise pressure distributions are calculated for several morphed sections. Finally, by taking into account the effect of pressure loads, the magnitudes of the required actuation forces are iteratively determined.

Nomenclature

d = length of the cutout rib (varies between 6 and 10 cm).
c = length of the hingeless control surface (selected as 20 cm).
w = width of the representative hingeless control surface (selected as 6 cm).
s = chordwise distance that is measured from the trailing edge.
TE = wing (or representative section) trailing edge.
Δ_{TE} = deflection at the trailing edge measured normal to the chord line (defined positive down).
d.o.f. = degrees-of-freedom.
MPC = multipoint constraint.
AC = aerodynamic center of the wing section.
c_l, c_m, c_d = airfoil lift, pitching moment (w.r.t. AC) and drag coefficients, respectively.
H = aerodynamic moment calculated for the hingeless control surface (6 by 20 cm) about a spanwise axis running along the rear spar.
F = magnitude of the actuation force.

$\Delta_{H=0}$ = trailing edge deflection of the morphed section that corresponds to zero aerodynamic moment case.

1 INTRODUCTION

In morphing wings designs, strategies to alter wing geometries [1,2] or eliminate slots and surface discontinuities in the control surfaces are employed to adaptively improve the aerodynamics and the structural response [9] within the complete flight envelope. Fixed wing geometry is mostly optimized for one design point, whereas the design criteria, i.e. Mach number, altitude, weight, change during the flight resulting in a decrease in the overall performance of the wing. Traditional control surfaces used in fixed geometry wings are very effective at the design condition where they provide the maximum benefit. However, they have minimal or no effect at the off-design conditions [10]. Mission adaptive wings provide a means to increase the efficiency criteria by better suiting the changing flight conditions, thus decreasing the fuel consumption [8]. By employing hingeless control surfaces in the design of mission adaptive wings, chordwise and spanwise variable camber can be implemented to improve the lift to drag ratio and to control the spanwise lift distribution, respectively [8]. In most application of this kind, conventional rib structures are replaced by actuation mechanisms to change the wing camber. The 'belt-rib' [6] approach uses multiple spokes instead of traditional ribs to permit camber bending of the wing section. Another approach uses ribs made out of rotating segments that are combined using revolute joints [8]. When the rib is deformed to desired shape, the skin follows the movement. Other designs are also based on the flexible rib concept where ribs are rotated to deflect the control surface section of the wing [4]. All these designs employ an open trailing edge, which reduces the structural stresses by letting the upper and lower skin panels to slide with respect to each other.

In this paper, a hingeless control surface concept is introduced and numerical analyses are performed to assess its structural and aerodynamic features. In these analyses several configurations are evaluated and the corresponding results are presented for comparative purposes. In the conclusion section, these results are discussed and configurations that are well balanced are identified.

2 CONCEPT DESCRIPTION

In terms of design philosophy, the concept studied in this paper employs the ideas discussed in references [4-8] to establish a solution that exploits the structural flexibility to change the wing aerodynamic camber. To accomplish this goal successfully, the final design is required to be reliable, lightweight and easy to manufacture using standard off-the-shelf components and standard engineering materials. In fact, the hingeless control surface will be manufactured mainly from $0.635\ mm$ thick Al2024-T3 panels.

Figure 1 shows the geometry of the rectangular wing with the hingeless control surfaces that is planned to be manufactured in later stages of the ongoing project. In order to ensure the flight safety, the unconventional structural modifications, such as the semi-open trailing edge and the rib cutouts, are only proposed for the hingeless control surfaces. The primary load carrying structure, i.e. the torque box, is a traditional design, which only requires minor modifications to

accommodate the hingeless control surfaces. Figure 2 shows the primary wing structure and components of the hingeless control surface on a representative wing section.

To change the wing camber using the hingeless control surface, actuators located in the torque box initiate a sliding motion at the slide-guide assemblies. The actuation forces are applied to the edges of the cutout ribs using flexible push rods which run along the lower control surface skin. Installation of the push rods requires small holes in the rear spar and the support webs. In future studies, these holes will be sized and reinforcements will be introduced if required.

Figure 3 shows the components of the guide-slide assembly, namely the cutout rib flange and the track that is connected to the lower skin. In addition to facilitating the sliding motion, the guide-assembly maintains the integrity of the hingeless control surface. Without it, the separation of lower and upper skins, which are not joined at the trailing edge, could not be prevented. It is considered that guide-slide assemblies will be manufactured from polycarbonate and lubricated to permit a smooth operation. Other studies [4,5,8] employ linear slide bearings to accommodate the sliding motion. In this concept, guide-slide assemblies are preferred since they also act as chordwise stringers. The total number of guide-slide assemblies required for a hingeless control surface of certain span is currently being investigated.

The relative motion initiated at the guide-slide assembly flexes the upper and lower control skins located between the cutout rib and the rear spar. In this concept, rib cutouts are used to introduce the structural flexibility required during camber changes. Since, the use of cutout ribs also introduces a structural weakness, support webs are employed to reinforce and stabilize the skins. The support webs are attached to upper and lower skin panels with hinge-type joints in a slanted fashion to be compatible with the kinematics of the camber changes. In the results section of this study, support web placement is discussed in detail.

The use of cutout ribs and the semi-open trailing edge in this concept increase the structural flexibility and reduce the structural stresses as well as the magnitudes of the actuation forces during camber changes. In the final design, the actuation system will be capable of controlling the increased flexibility and suppressing it when needed. Initial calculations show that commercially available actuators can meet the force requirements and are small enough to be fit in the torque box. Actuation force calculations are presented in the results section of this paper.

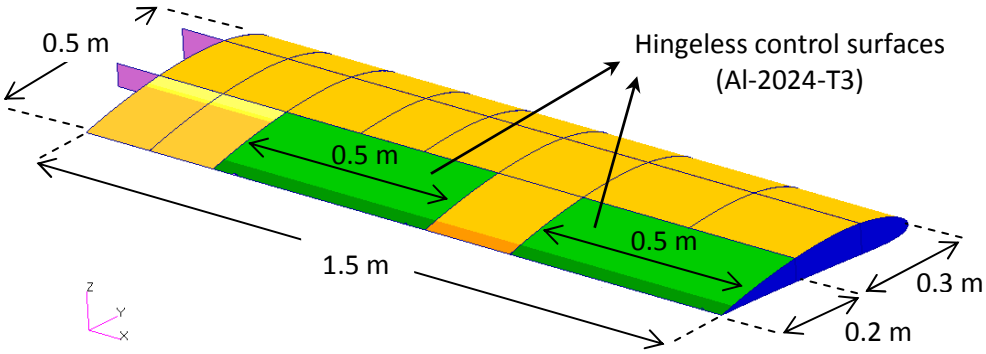

Figure 1: The rectangular wing with the hingeless control surfaces.

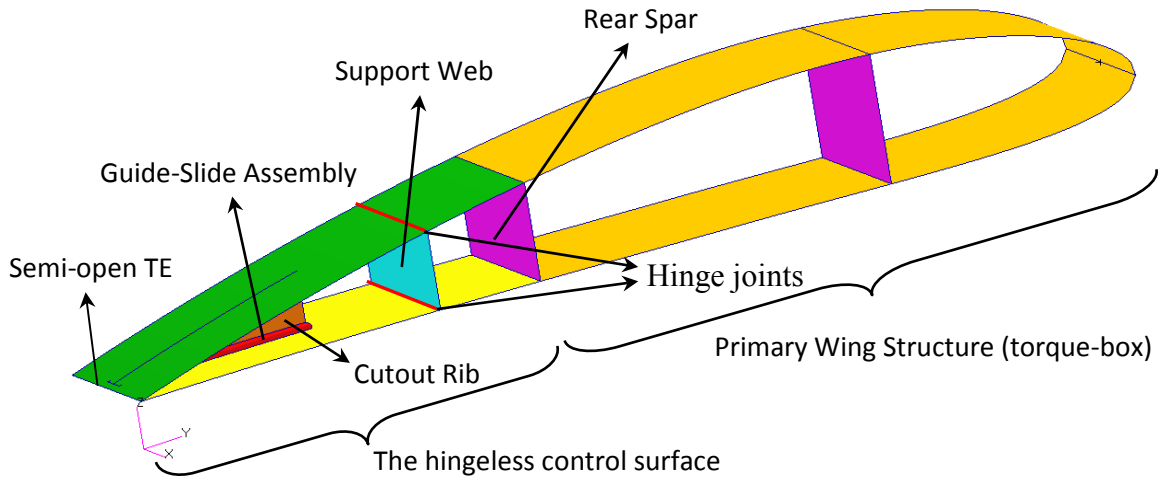

Figure 2: The representative wing section with the hingeless control surface.

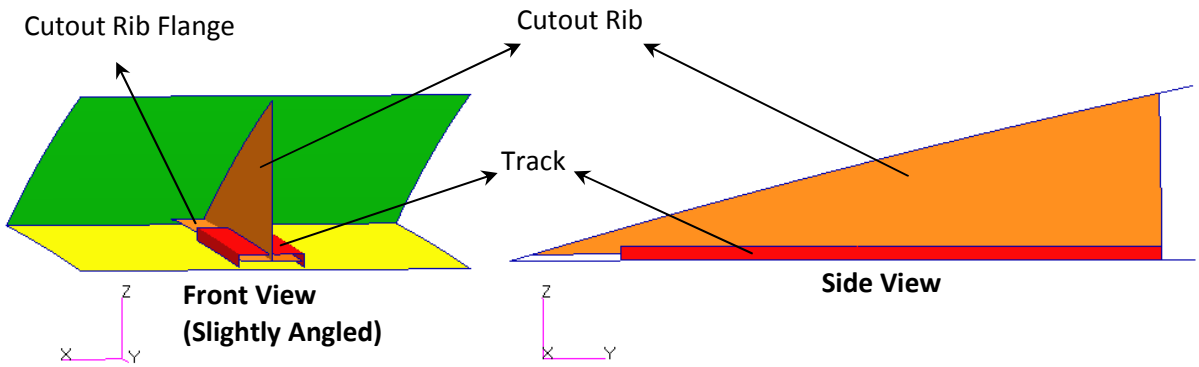

Figure 3: The guide-slide assembly of the hingeless control surface.

3 FEM MODELING

In order to evaluate the hingeless control surface concept discussed in the previous section, MSC® PATRAN is employed to create shell type finite element models of representative wing sections. Figure 4 shows one of these models where different components are color-coded and important parameters are defined. In these models, 4-node quadrilateral elements are used in an isometric mesh topology. Since the current study focuses on the hingeless control surface, the primary structure is excluded from the models and also the analysis.

By employing conforming mesh seeds, it is ensured that the isometric meshes created for the connected parts had coincident nodes along their edges. This conformity of meshes is essential in creating the rigid connections in the finite element model. After each part is meshed separately, the node equivalence is applied to eliminate the duplicate nodes and their corresponding degrees-of-freedom (d.o.f.). However, one must note that although rigid connections are created for all the adjoining parts, the upper and lower control surface skins are not joined along the trailing

edge in the models created. Thus, the most essential feature of this concept, which is the use of a semi-open section cell to change wing camber, is incorporated into the models.

In order to model the sliding motion created during the camber changes, double-sided contact elements are defined for the guide-slide assembly and the lower control surface skin as shown in Figure 4. In nonlinear analysis (*Solution 600, 'Implicit Nonlinear'*), the contact detection algorithm constrains the motion of the elements in a direction normal to their planes such that surface do not penetrate each other while sliding occurs along the tangential direction.

The nodes along the top and bottom edges of the support webs are coupled to those of upper and lower control surface panels using multipoint constraints (MPCs) to represent hinge-type joints where the rotational d.o.f. about the spanwise axis is unconstrained. In Figure 4, MPCs are represented by red lines with small circles. The use of MPCs allows the upper and lower control surfaces rotate about their hinge lines independently, as well as the support webs during camber changes.

The actuation force is applied at a node on the vertical edge of the cutout rib, which is located 5 mm above the lower control surface skin as shown in Figure 4 by the $\vec{F}$. The line of action of this force is selected such that it is initially parallel to the lower control surface in the plane of the wing cross section. Its point of application is selected such that the clearance needed for the pushrod fitting is provided. This force is modeled as a follower force, which mimics the behavior of the flexible push rods that are to be used in the design. As explained in the results section, the direction and magnitude of this force could be varied to achieve the desired positive and negative camber changes. In future studies, the reaction of the control force will be applied to the primary structure, where actuators are to be attached.

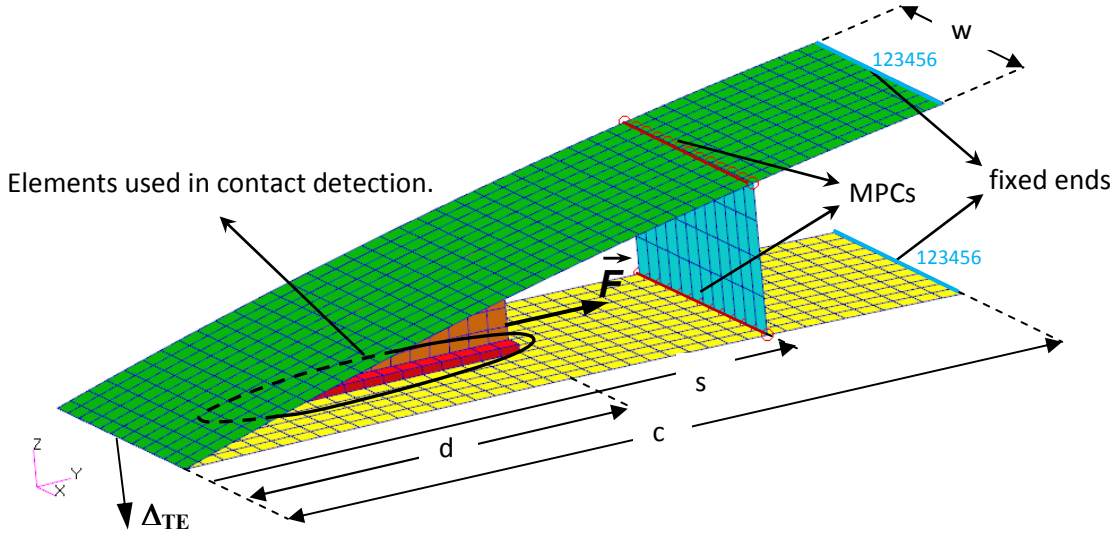

Figure 4: The finite element model of the hingeless control surface.

4 AERODYNAMIC MODELING

4.1 The CFD Solution

In this study, aerodynamic analyses of the representative wing sections are performed using ANSYS® FLUENT CFD software. In the solutions, structured C-grid aerodynamic meshes composed of quadrilateral elements are used. Figure 5 shows the computational domain and a typical solution mesh whose properties are listed in Table 1. The meshes used in this study are generated using the postprocessor tool GAMBIT of ANSYS® FLUENT. To ensure the consistency of the results corresponding to morphed sections, solution meshes are generated with identical nodal spacing at the boundaries. The contours of the morphed sections are determined from the finite element solutions, and spline functions are employed to accurately interpolate between nonconforming aerodynamic and structural node positions. Figure 6 shows the close-up views of the solution meshes corresponding to NACA 4412 airfoil and a morphed section corresponding to a finite element solution.

The CFD analyses performed in this study are based on the incompressible steady-state aerodynamics in two-dimensions. In these analyses, double precision option is employed and viscous effects are taken into account using the Spalart-Allmaras [11] turbulence model. Standard sea level atmospheric properties are used, i.e. $\rho = 1.225\ kg/m3$, $\nu = 1.7894x10^{-5}\ kg/m.s$, $P = 101.325\ kPa$ and the flight speed is selected as $U = 34\ m/s$, which corresponds to a Reynolds number of $Re \cong 950{,}000$.

Number of Cells	Number of Faces	Number of Nodes
12150	24555	12405

Table 1: CFD Mesh Details.

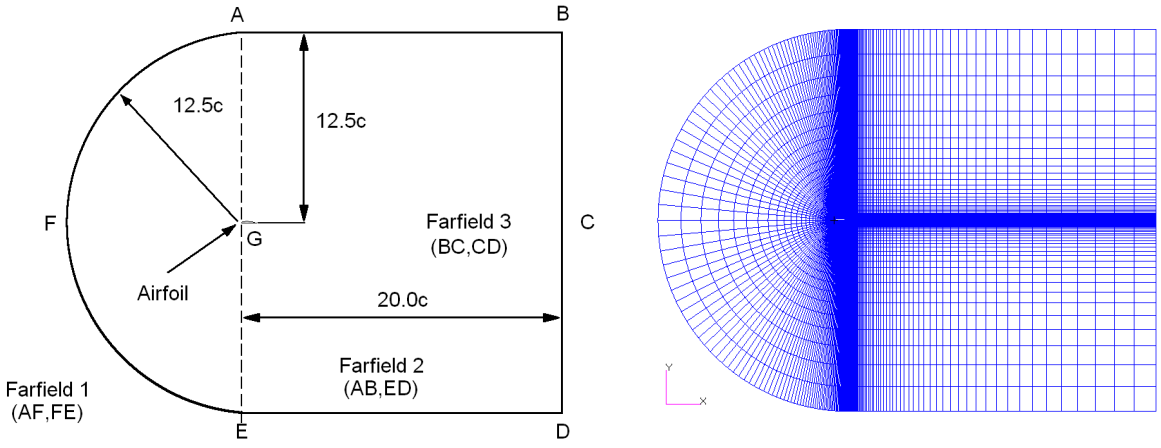

Figure 5: Solution domain and the C-grid solution mesh.

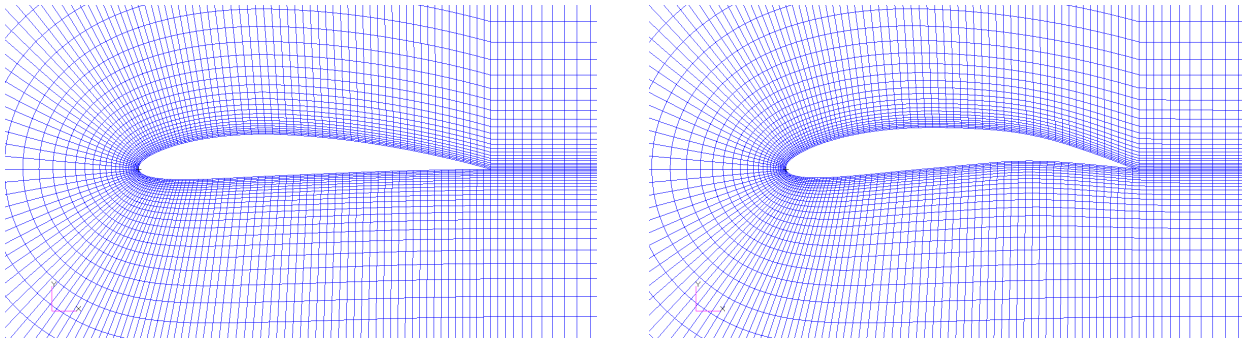

Figure 6: Close-up views of the NACA 4412 airfoil and a morphed section.

5 NUMERICAL RESULTS

5.1 Assessment of the Concept

In order to assess the hingeless control surface, finite element and CFD based structural and aerodynamic studies have been conducted for a $20\ cm$ hingeless control surface designed for a representative wing section of $6\ cm$ width and $50\ cm$ chord length. The main objective here is to determine the configuration which is well-balanced in terms of required control force as well as structural and aerodynamic performances.

As a first study, finite element models with cutout rib lengths of 6 to 14 cm are morphed, i.e. camber changes are applied, using a $10\ N$ actuation force. This force is applied to the models first along the positive chordwise direction to increase the aerodynamic camber, and then in negative chordwise direction to decrease it. In these analyses, the corresponding trailing edge deflections (Δ_{TE}) are calculated for each model. To simplify the analysis and to better interpret the results, support webs and aerodynamic forces are not yet included in the analyses. Figures 7a and 7b show the positive and negative trailing edge deflections corresponding to cases where aerodynamic camber is increased and decreased, respectively, by the application of the fixed magnitude actuation force in opposite directions. As seen in both figures, the magnitudes of calculated trailing edge deflections increase almost parabolically up to a limit with decreasing cutout rib length. In other words, for a fixed magnitude control force, if the cutout rib length decreases, the hingeless control surface deflects more at the trailing edge as it experiences a larger camber change. However, one must note that at the same time the structure becomes weaker since the length of the unsupported skin panels increases.

The variation of trailing edge deflection with the magnitude of the applied actuation force is also calculated in this study; Figures 8 shows the results. In this figure, the trailing edge deflections calculated for cutout rib lengths of 6 to $14\ cm$ are color coded as indicated by the legend. These deflections are within the expected operational range, where the structural nonlinearities are seen to be quite weak.

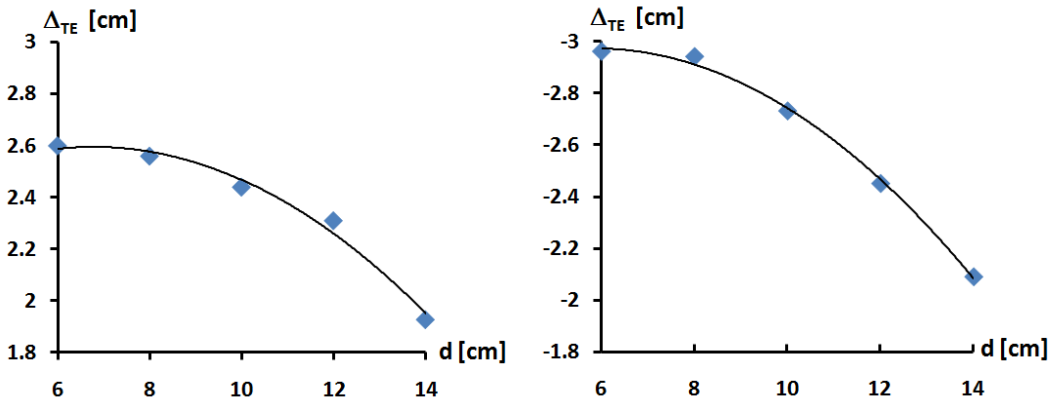

(a) $\vec{F}$ applied in positive and (b) negative chordwise directions.

Figure 7: Trailing edge deflections (Δ_{TE}) of the models with 6 to 14 cm cutout rib lengths (d) for an actuation force of 10 N applied in opposite directions.

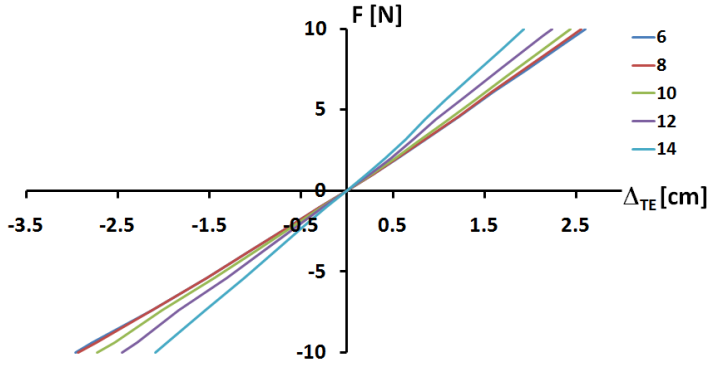

Figure 8: Actuation force (F) vs. trailing edge deflection (Δ_{TE}) shown for models with 6 to 14 cm cutout rib lengths.

The second study focuses on determining the support web orientation, which does not significantly constrain system during camber changes. Here, the analyses have been conducted only for the model with 10 cm cutout rib length by applying an actuation force of 10 N in positive chordwise direction. However, similar analyses can easily be performed for the other models if needed. In this study, runs have been performed using support webs which are slanted an angle θ with respect to vertical as shown in Figure 9a. In the models created, the upper edges of the support webs are connected to different locations on the upper surface while the lower edge is connected to the middle of the opening introduced by the cutout ribs. As discussed earlier, in these connections MPCs representing hinge-type joints are employed. Figure 9b shows the percent reduction of the trailing edge deflections caused by the use of the slanted support webs for an actuation force of 10 N.

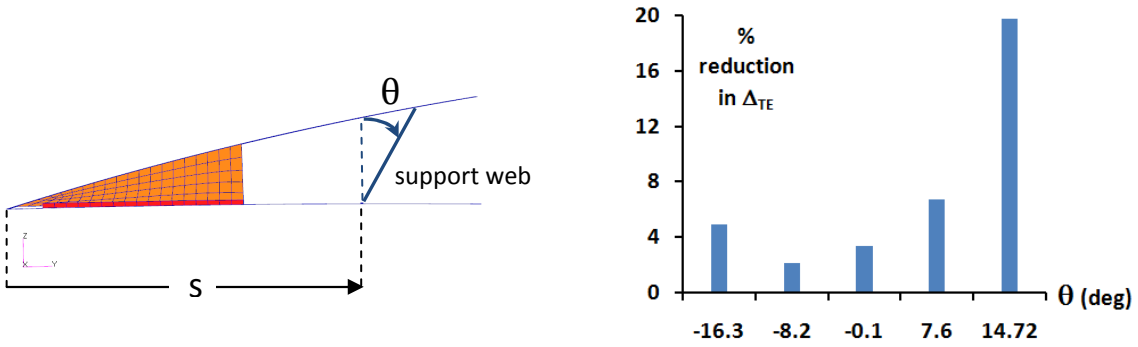

(a) **(b)**

Figure 9: Single support web case with 10 N actuation force: % reduction in the TE deflections vs. the support web angle.

From Figure 9b, one may observe that if slanting of the support webs is not introduced or incorrectly applied, the magnitudes the calculated trailing edge deflections decrease for a fixed magnitude actuation force. This may be explained by referring to Table 2, which compares $L_{initial}$ and L_{final} values for the model with no support web. These values represent the distances between upper surface and lower surface nodes for different θ values, before and after the deformations take place. If the percent change in distance is small for a certain θ value (identified by the highlighted rows in Table 2), it is observed that the support web placed along these nodes does not significantly constrain the system. This way, the desired amount of camber change may be achieved without attenuating useful actuation energy as the structure becomes unnecessarily strained. Table 3 presents similar results obtained for the two support web case, where the rows corresponding to smallest change in distance are once again highlighted.

As a final study in the assessment process, CFD based aerodynamic analyses are performed using the contours of the models with cutout rib lengths of 6 to 14 cm, which are morphed by an actuation force of 10 N. Currently, the effect of angle of attack is not yet considered, i.e. it is set to be zero. Figures 10a and 10b show the variation of lift and pitching moment coefficients with respect to calculated trailing edge deflections for the morphed sections. Likewise, in Figure 11, the variation of drag coefficient with respect to lift coefficient is presented for the morphed sections. In these plots, two data points, which are color coded according to the legend, are obtained for each model with different cutout rib lengths. These two points correspond to solutions where the wing camber is increased and decreased, respectively, by the fixed magnitude actuation force applied in opposite directions.

In Figures 10a and 10b, the data points for lift and pitching moment coefficients are observed to be distributed in very close proximity of straight lines. This behavior may be attributed to the flow characteristics, i.e. camber changes are small enough not to cause significant flow separation and nonlinear effects are relatively weak. According to the results of these CFD runs, it is possible to say that the lift and pitching moment coefficients are mostly affected by the change in the aerodynamic camber, which is directly proportional to the trailing edge deflections. In other words, these coefficients are seen to be quite insensitive to the actual shape of the morphed sections for the flow conditions investigated.

θ (degrees)	$L_{initial}$ (cm)	L_{final} (cm)	$\|\Delta L\|/ L_{initial}$ (%)
-16.3	3.585	3.513	1.999
-8.2	3.562	3.544	0.508
-0.1	3.609	3.640	0.872
7.6	3.723	3.797	2.002
14.7	3.898	4.007	2.813

Table 2: Single support web case (Web is located at $s = 15\ cm$).

	θ (degrees)	$L_{initial}$ (cm)	L_{final} (cm)	$\|\Delta L\|/ L_{initial}$ (%)
Web 1	-17.3	3.386	3.301	2.494
	-8.7	3.360	3.340	0.600
	-0.1	3.409	3.449	1.179
	8.0	3.528	3.621	2.639
	15.5	3.712	3.848	3.682
Web 2	-14.7	3.969	3.920	1.231
	-7.4	3.949	3.934	0.386
	-0.1	3.992	4.006	0.360
	6.9	4.096	4.135	0.948
	13.5	4.256	4.313	1.350

Table 3: Double support web case (Webs are located at $s_1 = 14$ cm and $s_2 = 17$ cm, respectively).

In Figure 11, the lift and drag coefficients corresponding to models with different cutout rib lengths are observed to be tightly clustered around a parabolic shape, which resembles a typical airfoil 'drag polar' curve. This behavior once again shows the strong dependence of these aerodynamic coefficients to the section camber and the insensitivity to the actual morphed shape.

In future studies, aerodynamic analyses will be performed to investigate a broad range of angle of attacks and larger TE deflections, where viscous effects are expected to be more dominant.

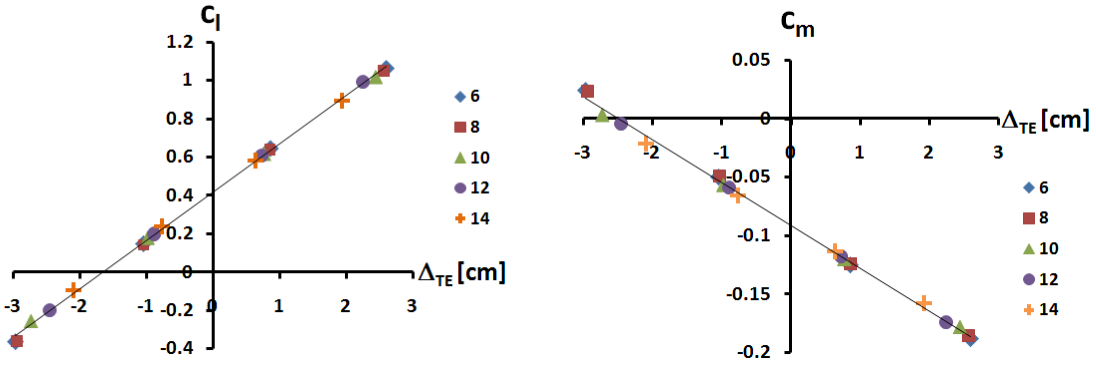

(a) (b)

Figure 10: (a) Lift and (b) pitching moment (w.r.t. AC) coefficients vs. TE deflection (Δ_{TE}) for morphed sections with 6 to 14 cm cutout rib length at zero angle of attack.

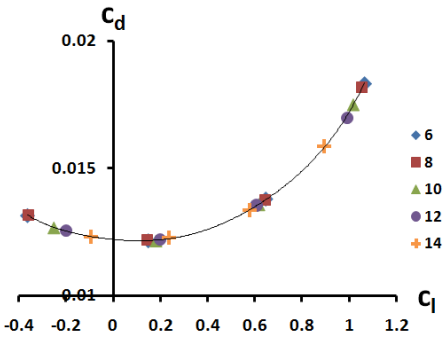

Figure 11: Lift vs. drag coefficients for morphed sections with 6 to 14 cm cutout rib length.

5.2 Results of the Coupled Structural and Aerodynamic Analysis

The 6 cm by 20 cm hingeless control surface model with the 10 cm cutout rib length and single support web of $\theta = -8.2^o$ is selected for further structural analysis in the presence of aerodynamic loads. One may note that in the second study of the previous section, this model was observed to be the most compatible with the deformation kinematics.

Figures 12a to 12e show the chordwise static pressure distributions calculated for the morphed states of the selected model at zero angle of attack conditions. In these figures, 's' defines the chordwise coordinate, which is measured from the trailing edge. To include the aerodynamic loads in the finite element model, the upper and lower surface pressure distributions are interpolated using polynomial functions between $s = 0$ and $s = 20\ cm$. These polynomials are then used to define the fields corresponding to pressure distributions in MSC® PATRAN using scalar PCL (PATRAN Command Language) functions. Since this study focuses on representative wing sections, the variation of pressure in spanwise direction is ignored.

The structural analyses are performed after the chordwise pressure distribution shown in Figures 12a to 12e are mapped onto the selected finite element model with the aforementioned properties. One must note that each of these five pressure distributions is only accurate for the corresponding morphed section with a particular trailing edge deflection. The values of these trailing edge deflections are listed below Figures 12a to 12e for each pressure distribution. In the analysis performed, the magnitude of the actuation force applied to the model is increased in an iterative fashion. The iterations continue until the trailing edge deflection calculated for the finite element model converges to that of the morphed section from which the pressure distribution is mapped from. At the end of this process, it is observed that the contours obtained from the finite element model matches that of the morphed section very accurately, i.e. aerodynamic loads do not create significant local deformations. Thus, aerodynamic calculations are not repeated or structural modifications are not introduced. Figures 13a-c and 14 show the Cauchy stress plots and superposed views of the morphed cross sections, respectively, corresponding to $\Delta_{TE} = -2.41, 0$ and 2.4 cm. Stress distributions displayed in Figure 13a to 13c show values that are well within the yield stress of Al2024-T3.

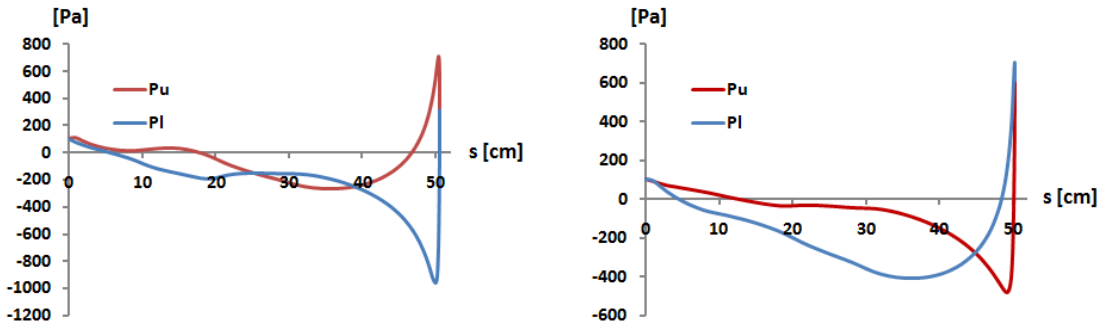

(a) $\Delta_{TE} = -2.41$ cm (b) $\Delta_{TE} = -0.977$ cm

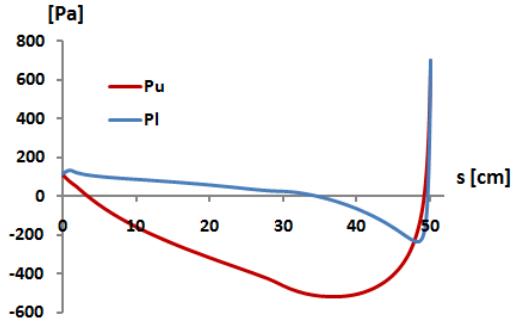

(c) $\Delta_{TE} = 0$ (corresponds to NACA 4412 airfoil)

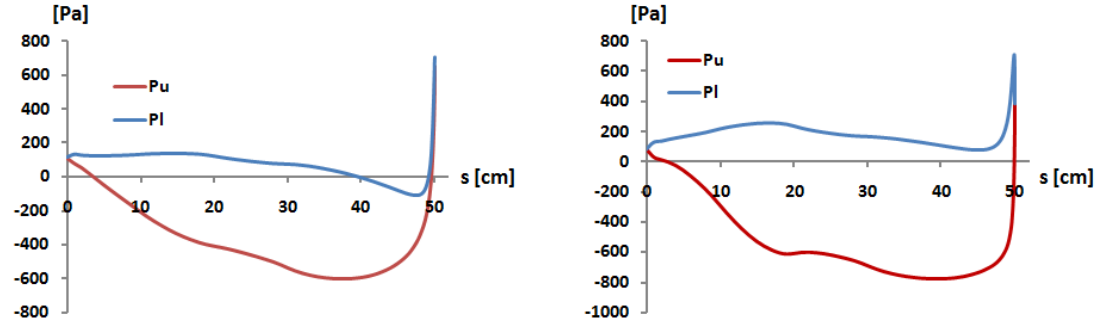

(d) $\Delta_{TE} = 0.81$ cm (e) $\Delta_{TE} = 2.4$ cm

Figure 12: Chordwise static pressure (gage) distributions for the morphed section with the 10 cm cutout rib length and single support web of $\theta = -8.2^{o}$ at zero angle of attack.

Figure 15 shows the variation of the actuation force with the trailing edge deflection for the model under consideration. Here, the blue and red markers represent the results obtained from the solutions for which the aerodynamic loads are excluded and included, respectively. The green markers show the difference between these two types of actuation forces. One may note that when $\Delta_{TE} = 0$, the magnitude of the actuation force in the presence of aerodynamic loads is approximately equal to 3.3 N. So, even when the hingeless control surface is undeformed, i.e. the cross section is the NACA 4412 profile, $F = 3.3\ N$ is required counteract the aerodynamic loads and to maintain the shape of the cross section the same.

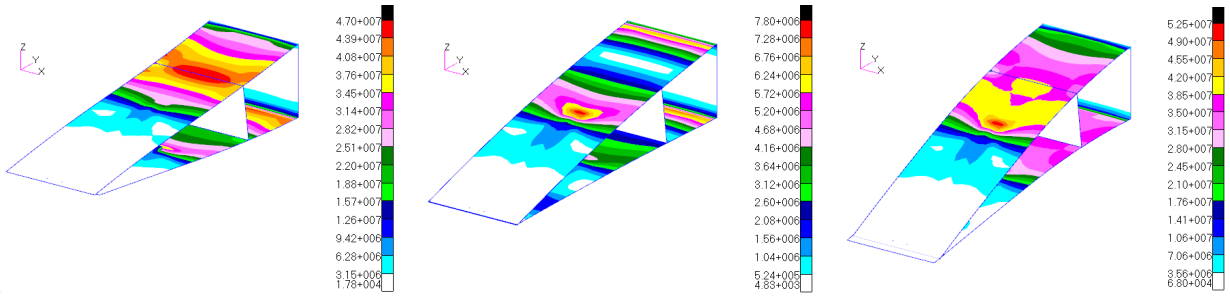

(a) $\Delta_{TE} = -2.41$ cm (b) $\Delta_{TE} = 0$ (c) $\Delta_{TE} = 2.4$ cm

Figure 13: Cauchy stress distributions (Pa) for the morphed model with the 10 cm cutout rib length and single support web of $\theta = -8.2^{o}$.

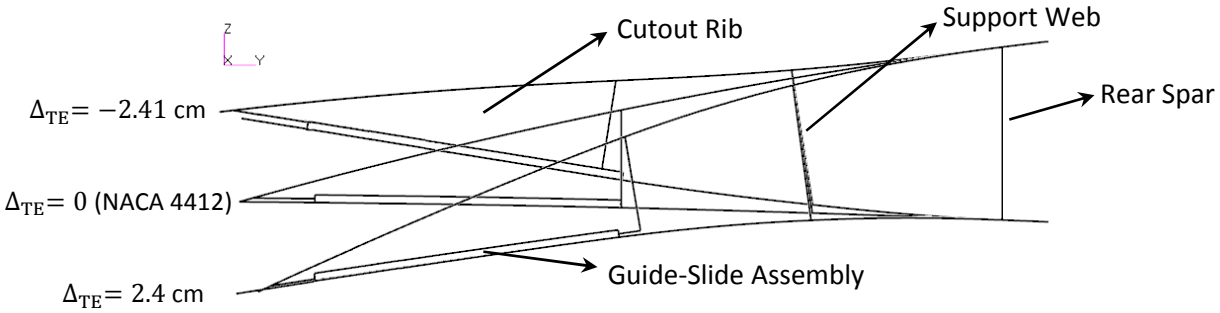

Figure 14: Superposed views of the morphed hingeless control surfaces as obtained from the finite element model with the 10 cm cutout rib length and single support web of $\theta = -8.2^{o}$.

From Figure 15, it is also possible to note that the trend lines corresponding to blue and red markers intersect each other and the trend line of the green markers crosses zero at $\Delta_{TE} \cong -1.7$ cm. This significance of this deflection value may be defined further by referring to Figure 16. This figure shows the variation of the aerodynamic moment 'H' with respect to the trailing edge deflection. The aerodynamic moment of the hingeless control surface is calculated by considering the effect of pressure loads about a spanwise axis located at the rear spar. Figure 16 shows that the aerodynamic moment becomes zero at $\Delta_{TE} \cong -1.7$ cm. This deflection value, which corresponds to a zero aerodynamic moment is be referred to as $\Delta_{H=0}$.

5 CONCLUDING REMARKS

In this paper, a hingeless control surface concept is introduced and numerical analyses are performed to assess its structural and aerodynamic aspects.

In the structural analyses performed, the finite element method is employed and several configurations with varying cutout rib lengths are investigated. The main observation here is that even though the finite element model is based on a nonlinear formulation, the results obtained show a linear behavior for the expected operational range. In addition, it is observed that the results obtained indicate that the use of shorter cutout rib lengths increase the flexibility of the design during camber changes. In other words, the hingeless control surface model with shorter cutout ribs experience larger camber changes for an actuation force of fixed magnitude compared to ones with longer cutout ribs. However, at the same time, use of shorter cutout ribs also results

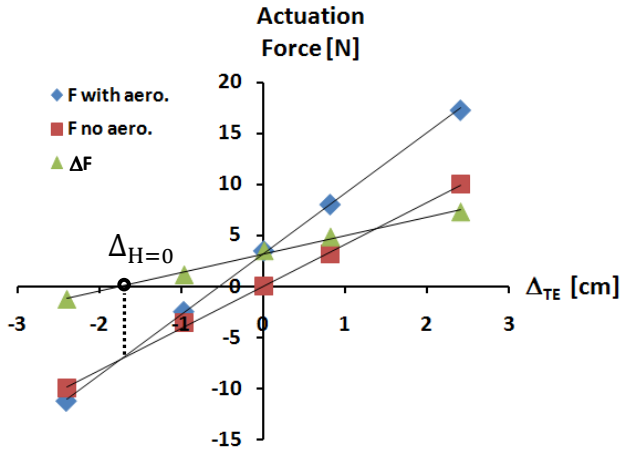

Figure 15: Variation of the actuation force with the trailing edge deflection (Δ_{TE}) for the model with the 10 cm cutout rib length and single support web of $\theta = -8.2^o$.

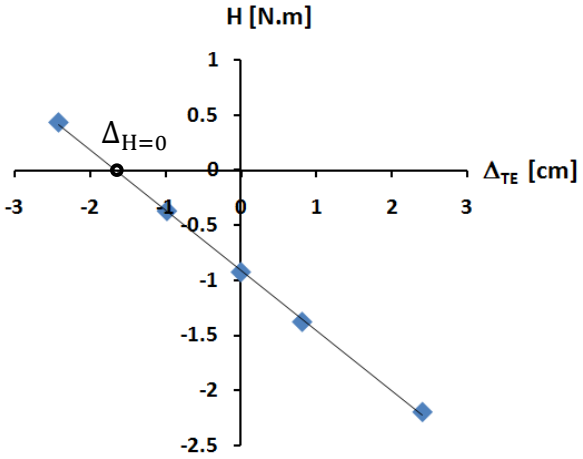

Figure 16: Variation of the aerodynamic moment (H) with the trailing edge deflection (Δ_{TE}) for the model with the 10 cm cutout rib length and single support web of $\theta = -8.2^o$.

in larger unsupported panels, which are more likely to encounter strength and structural stability problems.

To reinforce the unsupported panels, slanted support webs are used. These slanted support webs are connected to the upper and lower skin panels of the hingeless control surface using hinge-type connections. These hinge-type connections are created using MPCs and they only allow for free rotation about an axis parallel to the spanwise direction. In the analyses performed, it is observed that slanting the support webs and using hinge-type connections are required to avoid constraining the motion of the structure during camber changes.

CFD analyses are performed for the morphed sections whose geometries are determined from the finite element solutions. The results obtained indicate that the aerodynamic coefficients have a strong dependence on the camber increase, and are relatively insensitive to the actual deformed

shape. The chordwise pressure distributions obtained in these solutions are used to perform the final study.

To conduct the final study, the hingeless control surface model with the 10 cm cutout rib length and single support web is selected due to its well balanced characteristics. In each analysis, the pressure distribution obtained for a particular CFD analysis is mapped onto the finite element model. Then iterative solutions are performed to determine the corresponding actuation force magnitude. The iterations stop when the contour of the deformed model matches that of the morphed section from which the aerodynamic loads are determined from. From the results obtained, the deflection corresponding to zero aerodynamic moment is also determined. Cauchy stress values are also calculated for the hingeless control surface in this study. These values are seen to be well within yield limit of Al2024-T3, the material from which the hingeless control surface will be manufactured from.

The hingeless control surface concept studied in this paper relies on a relatively simple idea and a lightweight structural design, which allows it to be easily manufactured from off the shelf components and readily available materials. It can be applied to wings with unsymmetrical airfoils such as the NACA 4412 chosen for this study, as well as symmetrical ones. Also, integration of this concept into existing wing structures can be done conveniently, since major modifications are not required in the torque box. From the numerical results, it is observed that both positive and negative camber changes can be accommodated with similar magnitude actuation forces, i.e. the structure is not more 'selective' towards positive or negative camber changes. In the expected range of operation, both the structural and the aerodynamic models predict linear behavior, even though nonlinear effects are fully included in the formulations. Although further research may involve analyses in the nonlinear range, the use of simplified linearized models seem promising when the studies are extended to three-dimensional wings for which optimization and aeroelastic analysis are to be conducted. Another topic to be investigated in the near future may involve the use of alternative materials for the flexing skin panels, such as corrugated composites, to lower the actuation force magnitudes further.

In light of the preliminary results obtained in this study, it is believed that the hingeless control surface concept introduced in this paper has the potential to be used in morphing wing applications. Future work will be conducted to fully explore this concept and introduce additional improvements that may be required.

ACKNOWLEDGEMENT

This research was supported by Turkish Scientific and Technological Research Council through the project 'TUBITAK/107M103, Aeroservoelastic Analysis of the Effects of Camber and Twist on Tactical Unmanned Aerial Vehicle Mission-Adaptive Wings'. The authors gratefully acknowledge the support given.

REFERENCES

[1] Bowman, J., Sanders, B., Cannon, B.,Kudva, J., Joshi, S., Weisshaar, T., Development of Next Generation Morphing Aircraft Structures, 48th AIAA/ASME/ASCE/AHS/ASC Structures, Structural Dynamics, and Materials Conference, 2007.
[2] Bye, D.R., McClure, P.D., Design of a Morphing Vehicle, 48th AIAA/ASME/ASCE/AHS/ ASC Structures, Structural Dynamics, and Materials Conference, 2007.
[3] Andersen, G.R., Cowan, D.L., Aeroelastic Modeling, Analysis and Testing of a Morphing Wing Structure, AIAA/ASME/ASCE/AHS/ASC Structure, Structural Dynamics. And Materials Conference, 2007.
[4] Masarati, M., Quaranta, G., Ricci, S. and Scotti, A., Aeroservoelastic Analysis of Morphing Controlled Surfaces, IFASD 2007-055, 2007.
[5] Ricci, S., Scotti, A. and Terraneo, M., Design, Manufacturing and Preliminary test Results of an Adaptive Wing Camber Model, AIAA/ASME/ASCE/AHS/ASC Structures, Structural Dynamics, and Materials Conference, 2006.
[6] Campanile, L.F. and Anders, S., Aerodynamic and Aeroelastic Amplification in Adaptive Belt-rib Airfoils, Aerospace Science and Technology, 9(1), 55–63, 2005.
[7] Gern, F.H., Inman, D.J., Kapania, R. K., Structural and Aeroelastic Modeling of General Planform Wings with Morphing Airfoils, AIAA Journal, 40(4), 628-637, 2002.
[8] Monner, H. S., Realization of an Optimized Wing Camber by Using Formvariable Flap Structures, Aerospace Science and Technology, 5, 445–455, 2001.
[9] Stanewsky, E., Adaptive Wing and Flow Control Technology, Progress in Aerospace Sciences, 37, 583–667, 2001.
[10] Stanewsky, E., Aerodynamic Benefits of Adaptive Wing Technology, Aerospace Science and Technology, 4, 439–452, 2000.
[11] Spalart, P. R., Allmaras, S. R., 'A One-Equation Turbulence Model for Aerodynamic Flows', AIAA Paper 92-0439, 1992